

Supporting Information

A microporous lanthanide-tricarboxylate framework with potential for purification of nature gas

Yabing He,^a Shengchang Xiang,^b Zhangjing Zhang,^b Shunshun Xiong,^a Frank R. Fronczek,^c Rajamani Krishna,*^d Michael O'Keeffe^e and Banglin Chen*^a

^a Department of Chemistry, University of Texas at San Antonio, One UTSA Circle, San Antonio, Texas 78249-0698, United States; Fax: (1)-210-458-7428; E-mail: Banglin.Chen@utsa.edu; Homepage: www.utsa.edu/chem/chen.html

^b Fujian Provincial Key Laboratory of Polymer Materials, Fujian Normal University, 3 Shangsan Road, Cangshan Region, Fuzhou 350007, China

^c Department of Chemistry, Louisiana State University, Baton Rouge, LA 70803-1804, United States

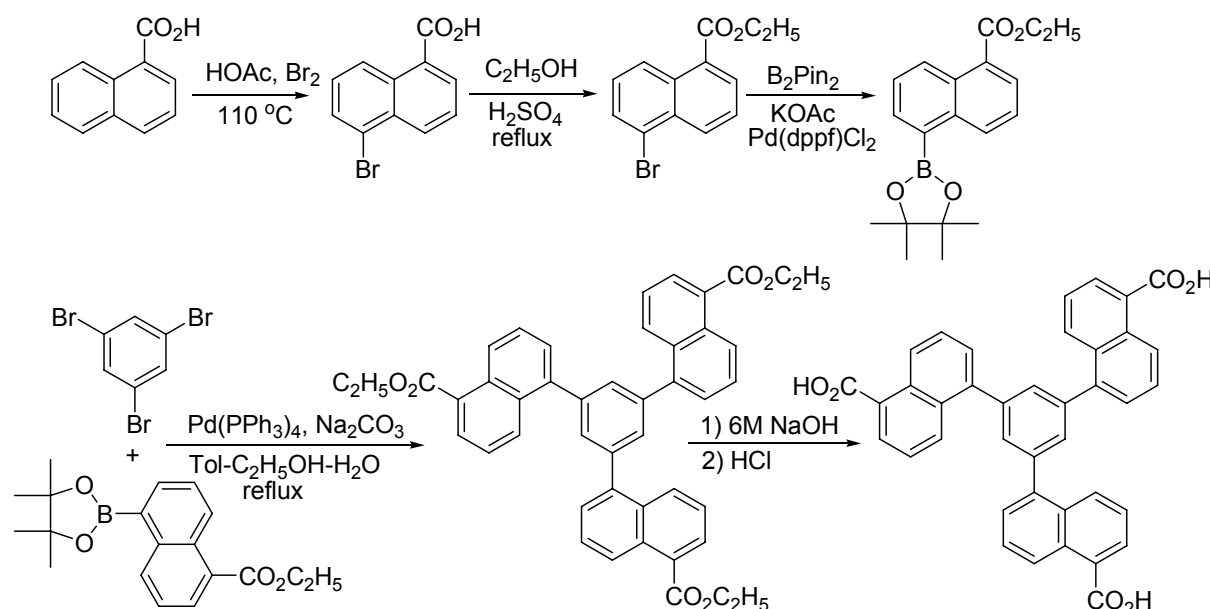
^d Van 't Hoff Institute for Molecular Sciences, University of Amsterdam, Science Park 904, 1098 XH Amsterdam, The Netherlands; E-mail: R.Krishna@uva.nl

^e Department of Chemistry and Biochemistry, Arizona State University, Tempe, Arizona 85287-1604, United States

1. General remark

All reagents and solvents were used as received from commercial suppliers without further purification. ¹H NMR and ¹³C NMR spectra were recorded on a Varian Mercury 300 MHz spectrometer. Tetramethylsilane (TMS) and deuterated solvents (CDCl₃, δ = 77.00 ppm; DMSO-d₆, δ = 39.50 ppm) were used as internal standards in ¹H NMR and ¹³C NMR experiments, respectively. The coupling constants were reported in Hertz. FTIR spectra were performed on a Bruker Vector 22 spectrometer at room temperature. The elemental analyses were performed with Perkin–Elmer 240 CHN analyzers from Galbraith Laboratories, Knoxville. Thermogravimetric analyses (TGA) were measured using a Shimadzu TGA-50 analyzer under a nitrogen atmosphere with a heating rate of 3 °C min⁻¹. Powder X-ray diffraction (PXRD) patterns were recorded by a Rigaku Ultima IV

diffractometer operated at 40 kV and 44 mA with a scan rate of 1.0 deg min⁻¹. The crystallographic measurement was made on a Bruker SMART Apex II CCD-based X-ray diffractometer system equipped with a Mo-target X-ray tube ($\lambda = 0.71073 \text{ \AA}$) operated at 2000 watts power (50 kV, 40 mA). The structure was solved by direct method and refined to convergence by least squares method on F^2 using the SHELXTL software suit. A Micromeritics ASAP 2020 surface area analyzer was used to measure gas adsorption isotherms. To have a guest-free framework, the fresh sample was guest-exchanged with dry acetone at least 10 times, filtered and vacuumed at room temperature (296 K) until the outgas rate was 5 $\mu\text{mHg min}^{-1}$ prior to measurements. A sample of 84.2 mg was used for the sorption measurements and was maintained at 77 K with liquid nitrogen, at 273 K with an ice–water bath. As the center-controlled air conditioner was set up at 23 °C, a water bath was used for adsorption isotherms at 296 K.



Scheme S1. The synthetic route to the organic linker H_3L .

2. Synthesis and characterization of the organic building block (H_3L)

5-Bromonaphthalene-1-carboxylic acid¹: To a suspension of naphthalene-1-carboxylic acid (20.00 g, 116.2 mol, Alfa Aesar) in glacial acetic acid (100 mL, Sigma Aldrich) was added dropwise bromine (6.6 mL, 128.4 mmol, Acros). The mixture was then heated to 110 °C and stirred at this temperature for 48 hrs. After cooled to room temperature, the mixture was filtered, washed with *n*-hexane, and dried to give 5-bromonaphthalene-1-carboxylic acid as a grey solid (17.70 g, 70.5 mmol, 61%). ¹H NMR (DMSO-*d*₆, 300.0 MHz) δ (ppm): 13.30 (s, br, 1H), 8.85 (d, *J* = 8.7 Hz,

1H), 8.39 (d, J = 8.4 Hz, 1H), 8.20 (d, J = 7.2 Hz, 1H), 7.97 (d, J = 7.5 Hz, 1H), 7.75 (m, 1H), 7.55 (m, 1H).

Ethyl 5-bromo-1-naphthoate: ^1H NMR (CDCl_3 , 300.0 MHz) δ (ppm): 8.90 (d, J = 8.7 Hz, 1H), 8.48 (d, J = 8.4 Hz, 1H), 8.21 (d, J = 7.2 Hz, 1H), 7.84 (d, J = 7.5 Hz, 1H), 7.60 (m, 1H), 7.43 (m, 1H), 4.50 (q, J = 6.9 Hz, 2H), 1.49 (t, J = 6.9 Hz, 3H).

Ethyl 5-(pinacolboryl)-1-naphthoate: This compound was prepared according to the literature.²

5,5'5"-Benzene-1,3,5-triyl-1,1',1"-trinaphthoic acid (H_3L)³: To a mixture of 1,3,5-tribromobenzene (2.41 g, 7.66 mmol), ethyl 5-(pinacolboryl)-1-naphthoate (10.00 g, 30.65 mmol), Na_2CO_3 (9.74 g, 91.89 mmol), and $\text{Pd}(\text{PPh}_3)_4$ (0.89 g, 0.77 mmol) were added degassed mixed solvents (toluene/ethanol/ H_2O : 100/50/50 mL). The resulting mixture was stirred under reflux under a nitrogen atmosphere for 48 hrs. After removal of the solvents, CH_2Cl_2 (150 mL) and H_2O (80 mL) were added. The organic phase was separated and the aqueous phase was extracted with CH_2Cl_2 (80 mL \times 2). The combined organic phase was washed with brine (80 mL), dried over anhydrous MgSO_4 , and concentrated in vacuo. The residue was purified by silica gel column chromatography using CH_2Cl_2 as eluent to give triethyl ester intermediate in 77 % yield, which was hydrolyzed with 6 M NaOH to afford the title compound in quantitative yield. ^1H NMR (DMSO- d_6 , 300.0 MHz) δ (ppm): 13.24 (s, br, 3H), 8.88 (dd, J = 7.5 Hz, 2.1 Hz, 3H), 8.35 (d, J = 8.4 Hz, 3H), 8.14 (dd, J = 7.2 Hz, 1.2 Hz, 3H), 7.61-7.76 (m, 12H); ^{13}C NMR (DMSO- d_6 , 75.4 MHz) δ (ppm): 168.64, 140.23, 139.21, 131.15, 130.91, 130.47, 129.91, 129.43, 128.52, 127.59, 126.93, 125.42, 125.36; Selected FTIR (neat, cm^{-1}): 1674, 1611, 1575, 1510, 1466, 1414, 1382, 1325, 1232, 1195, 1160, 1124, 1055, 1007, 975, 918, 890, 874, 851, 788, 766, 709.

3. Synthesis and characterization of UTSA-30

The organic linker H_3L (10.0 mg, 17.0 μmol) and $\text{Yb}(\text{NO}_3)_3 \cdot 5\text{H}_2\text{O}$ (20.0 mg, 44.5 μmol , Aldrich) were dissolved in *N,N'*-dimethylacetamide (DMA) (2.0 mL) in a disposable scintillation vial (20 mL). The vial was capped tightly and placed at an oven at 110 °C for 48 h. The colorless block-shaped crystals were collected by filtration and washed with DMA in 55% yield. **UTSA-30** can be formulated as $[\text{Yb}(\text{L})]3\text{DMA}$ on the basis of single-crystal X-ray structure determination, TGA, and microanalysis. Selected FTIR (neat, cm^{-1}): 1639, 1612, 1577, 1528, 1510, 1462, 1417, 1378, 1346, 1324, 1260, 1177, 1152, 1092, 1057, 1010, 891, 862, 843, 808, 792, 781, 749, 723, 700,

675; TGA data: Calcd. weight loss for 3DMA: 25.6%, Found: 25.5%; Elemental analysis: Calcd for C₅₁H₄₈N₃O₉Yb: C 60.05, H 4.74, N 4.12%; found: C 59.98, H 5.00, N 4.08%.

4. Fitting of pure component isotherms

The measured experimental data on pure-component isotherms for CH₄, C₂H₂, C₂H₄, C₂H₆, C₃H₆, C₃H₈, CO₂, and N₂ at temperatures of 273 K and 296 K in **UTSA-30a** were first converted to *absolute* loading using the Peng-Robinson equation of state for estimation of the fluid densities. The pore volumes used for this purpose is 0.2594 cm³ g⁻¹. The pure-component isotherm data for CH₄, C₂H₂, C₂H₄, C₂H₆, C₃H₆, C₃H₈, CO₂, and N₂, expressed in terms of *absolute* loadings, were fitted with the dual-site Langmuir (DSL) isotherm model

$$q \equiv q_A + q_B = \frac{q_{sat,A} b_A p}{1 + b_A p} + \frac{q_{sat,B} b_B p}{1 + b_B p} \quad (1)$$

with *T*-dependent parameters b_A , and b_B

$$b_A = b_{A0} \exp\left(\frac{E_A}{RT}\right); \quad b_B = b_{B0} \exp\left(\frac{E_B}{RT}\right) \quad (2)$$

The fitted parameter values are presented in *Table S1*. As illustration of the goodness of the fits, *Figure S8* presents a comparison of absolute component loadings for CH₄, C₂H₂, C₂H₄, C₂H₆, C₃H₆, C₃H₈, CO₂, and N₂ at 296 K in **UTSA-30a** with the isotherm fits. The fits are good for all components over the entire pressure ranges. We note that the pure-component adsorption loadings follow the hierarchy: C₃ hydrocarbons (C₃H₆, C₃H₈) > C₂ hydrocarbons (C₂H₂, C₂H₄, C₂H₆) > CO₂ > CH₄ > N₂.

5. Isosteric heat of adsorption

The binding energies of CH₄, C₂H₂, C₂H₄, C₂H₆, C₃H₆, C₃H₈, CO₂, and N₂ in **UTSA-30a** are reflected in the isosteric heat of adsorption, Q_{st} , defined as

$$Q_{st} = RT^2 \left(\frac{\partial \ln p}{\partial T} \right)_q \quad (3)$$

These values were determined using the pure-component isotherm fits. *Figure S9* presents data on the loading dependence of - Q_{st} for the eight different guest molecules in **UTSA-30a**. We note that

the values of $-Q_{st}$ follow the hierarchy: $\text{C}_3\text{H}_6 > \text{C}_3\text{H}_8 > \text{C}_2\text{H}_2 \approx \text{C}_2\text{H}_4 \approx \text{C}_2\text{H}_6 > \text{CO}_2 > \text{CH}_4 > \text{N}_2$. This hierarchy is in line with the pure-component adsorption hierarchy observed in *Figure S8*.

6. IAST calculations of adsorption selectivities and uptake capacities

The data on the pure-component isotherms, along with the isosteric heats of adsorption, indicate that it is possible to recover pure methane from a mixture containing a wide variety of impurities such as C_2H_2 , C_2H_4 , C_2H_6 , C_3H_6 , C_3H_8 , CO_2 , and N_2 . In order to establish the feasibility of this separation, we performed the calculations using the Ideal Adsorbed Solution Theory (IAST) of Myers and Prausnitz.⁴ The validity of IAST estimations of CO_2/CH_4 , CO_2/H_2 , CH_4/H_2 , and CO_2/N_2 mixture equilibria in a variety of MOFs (**MgMOF-74**, **MOF-177**, **BTP-COF**) and zeolites (**FAU**, **LTA**, **MFI**, **CHA**) has been established in earlier publications by comparison of IAST calculations with molecular simulations of binary adsorption equilibrium.⁵⁻⁹

Figure S10 presents IAST calculations of the component loadings for CH_4 , C_2H_2 , C_2H_4 , C_2H_6 , C_3H_6 , C_3H_8 , CO_2 , and N_2 in an 8-component equimolar mixture as a function of the total bulk gas phase pressure at 296 K. The IAST calculations show the component loadings in the mixture are bunched into five different sub-groups with the following loading hierarchies: C₃ hydrocarbons (C_3H_6 , C_3H_8) > C₂ hydrocarbons (C_2H_2 , C_2H_4 , C_2H_6) > CO_2 > CH_4 > N_2 .

Figure 3 in the paper presents calculations of the four different adsorption selectivities: CO_2/CH_4 , CH_4/N_2 , $(\text{C}_2\text{H}_6+\text{C}_2\text{H}_4+\text{C}_2\text{H}_2)/\text{CH}_4$, and $(\text{C}_3\text{H}_6+\text{C}_3\text{H}_8)/(\text{C}_2\text{H}_2+\text{C}_2\text{H}_4+\text{C}_2\text{H}_6)$ as a function of the total bulk gas phase pressure at 296 K. The calculations of the four different selectivities presented in *Figure 3* in the paper were based on the component loadings in an 8-component equimolar mixture. These selectivities are not significantly altered with changes in the composition of the mixture. In order to demonstrate this, we compared the four individual selectivities $(\text{C}_2\text{H}_6+\text{C}_2\text{H}_4+\text{C}_2\text{H}_2)/\text{CH}_4$, $(\text{C}_3\text{H}_6+\text{C}_3\text{H}_8)/(\text{C}_2\text{H}_2+\text{C}_2\text{H}_4+\text{C}_2\text{H}_6)$, CO_2/CH_4 , and CH_4/N_2 with those obtained from calculations for other mixtures. The comparisons are summarized in *Figure S11*. Firstly, let us compare the CO_2/CH_4 adsorption selectivities obtained from loadings in an 8-component mixture (filled red circles) with those for an equimolar 2-component CO_2/CH_4 mixture (open red circles). The two sets of values are only slightly altered at the higher pressures. Secondly, let us compare the CH_4/N_2 adsorption selectivities obtained from loadings in an 8-component mixture (filled pink inverted triangles) with those for an equimolar 2-component CH_4/N_2 mixture (open inverted triangles). The

two sets of values are only slightly altered at the higher pressures. Thirdly, let us compare the (C₂H₆+C₂H₄+C₂H₂)/CH₄ adsorption selectivities obtained from loadings in an 8-component mixture (filled blue triangles) with those for an equimolar 4-component CH₄/C₂H₂/C₂H₄/C₂H₆ mixture (open triangles). The two sets of values are practically identical for the entire range of pressures. Finally, let us compare the (C₃H₆+C₃H₈)/(C₂H₂+C₂H₄+C₂H₆), adsorption selectivities obtained from loadings in an 8-component mixture (filled stars) with those for an equimolar 5-component C₂H₂/C₂H₄/C₂H₆/C₃H₆/C₃H₈ mixture (open stars). The two sets of values are practically identical for the entire range of pressures.

From the comparisons of IAST calculations presented in *Figure S11*, we conclude that the adsorption selectivities are not significantly influenced by mixture compositions.

7. Pulse chromatographic simulations

We performed transient pulse chromatographic simulations following the methodologies developed and described in earlier works.^{9,10-14} *Figure S12* shows a schematic diagram of a packed bed adsorber bed of length L , packed with **UTSA-30a** crystals. Assuming plug flow of an n -component gas mixture through a fixed bed maintained under isothermal conditions, the partial pressures in the gas phase at any position and instant of time are obtained by solving the following set of partial differential equations for each of the species i in the gas mixture.^{9,12,14-16}

$$\frac{1}{RT} \frac{\partial p_i(t, z)}{\partial t} = - \frac{1}{RT} \frac{\partial(v(t, z)p_i(t, z))}{\partial z} - \frac{(1-\varepsilon)}{\varepsilon} \rho \frac{\partial q_i(t, z)}{\partial t}; \quad i = 1, 2, \dots, n \quad (4)$$

In equation (4), t is the time, z is the distance along the adsorber, ρ is the framework density, ε is the bed voidage, v is the interstitial gas velocity, and q_i is the molar loading within the crystallites. The framework density of **UTSA-30a** is 1082.4 kg m⁻³. The molar loadings q_i are calculated using IAST on the basis of adsorption equilibrium with the bulk gas phase partial pressures p_i at that position z and time t .

The *interstitial* gas velocity is related to the *superficial* gas velocity by

$$v = \frac{u}{\varepsilon} \quad (5)$$

Summing equation (4) over the n species present in the mixture, we obtain

$$\frac{1}{RT} p_t \frac{\partial(v(t, z))}{\partial z} = -\frac{(1-\varepsilon)}{\varepsilon} \rho \frac{\partial q_t(z)}{\partial z} \quad (6)$$

where we have involved the assumption of negligible pressure drop, i.e.

$$\frac{\partial p_t}{\partial z} = 0 \quad (7)$$

For simulation of pulse chromatographic separations, we use the set of inlet conditions

$$0 \leq t \leq t_0; \quad p_i(0, t) = p_{i0}; \quad u(0, t) = u_0 \quad (8)$$

where t_0 is the time for duration of the pulse.

Further details of the adsorber model, along with the numerical procedures used in this work, are provided by Krishna and co-workers.^{6,12-14} Typical computation times for a binary gas mixture breakthrough are less than 500 s, allowing such transient adsorber calculations to be routinely used for screening purposes.

Experimental validation of the chromatographic simulation methodology is provided in earlier works.^{9,12,14,17}

For the pulse chromatographic simulations, the following parameter values were used, as before, $L = 0.12$ m; $\varepsilon = 0.75$; $u = 0.00225$ m s⁻¹, together with a pulse duration $t_0 = 10$ s.

It is to be noted that the actual values of these parameters have no real bearing on the conclusions drawn on the separation performance and for this reason the simulation results for transient breakthrough are presented in our investigation in terms of a *dimensionless* time, τ , defined by dividing the actual time, t , by the characteristic time, $L\varepsilon/u_0$.

In order to demonstrate that the fractionation ability of **UTSA-30a** is independent of the chosen mixture compositions, we performed pulse chromatographic simulations for three additional mixtures: (a) an equimolar 3-component CH₄/CO₂/N₂ mixture, (b) an equimolar 4-component CH₄/C₂H₂/C₂H₄/C₂H₆ mixture, and (c) an equimolar 5-component C₂H₂/C₂H₄/C₂H₆/C₃H₆/C₃H₈ mixture. The three sets of pulse chromatographic simulation results are presented in *Figures S13a,b,c*

From *Figure S13a*, we note that **UTSA-30a** is able to fractionate a CH₄/CO₂/N₂ mixture even when higher hydrocarbons are not present. In other words, the fractionation of the individual components CH₄, CO₂, and N₂ does not depend on the mixture composition.

From *Figure S13b*, we note that **UTSA-30a** is able to fractionate a CH₄/C₂H₂/C₂H₄/C₂H₆ mixture to C₁ and C₂ streams. In other words, the fractionation of the ability of **UTSA-30a** to achieve C₁/C₂ separation does not depend on the presence, or absence, of CO₂, N₂ and higher hydrocarbons.

From *Figure S13c*, we note that **UTSA-30a** is able to fractionate a C₂H₂/C₂H₄/C₂H₆/C₃H₆/C₃H₈ mixture to C₂ and C₃ streams. In other words, the fractionation of the ability of **UTSA-30a** to achieve C₂/C₃ separation does not depend on the presence, or absence, of CO₂, N₂, and CH₄.

From the results presented in *Figure 4* in the paper and *Figures S13a,b,c*, we conclude the fractionation ability of **UTSA-30a** is not dependent on the chosen mixture composition.

8. Comparison of UTSA-30a with NaX zeolite

We now compare the separation performance of **UTSA-30a** for natural gas purification with traditionally used adsorbent **NaX** zeolite. For this purpose, we choose to separate a 3-component CH₄/C₂H₆/C₃H₈ mixture containing only the major components of natural gas. The isotherm parameter values for **NaX** zeolite were obtained from literature sources.¹⁸⁻²⁰ These are summarized in *Table S2*.

The filled symbols in *Figure S14* refer to the simulations for **UTSA-30a**. The open symbols in *Figure S14* are the corresponding ones for **NaX** zeolite. We note that the separation characteristics of both materials are nearly the same. The peaks for CH₄ and C₃H₈ with these two materials nearly coincide with each other. There is only a small difference at the times for emergence of the peaks of C₂H₆. We conclude from this comparison that the separation performance of **UTSA-30a** is comparable to that of **NaX** zeolite.

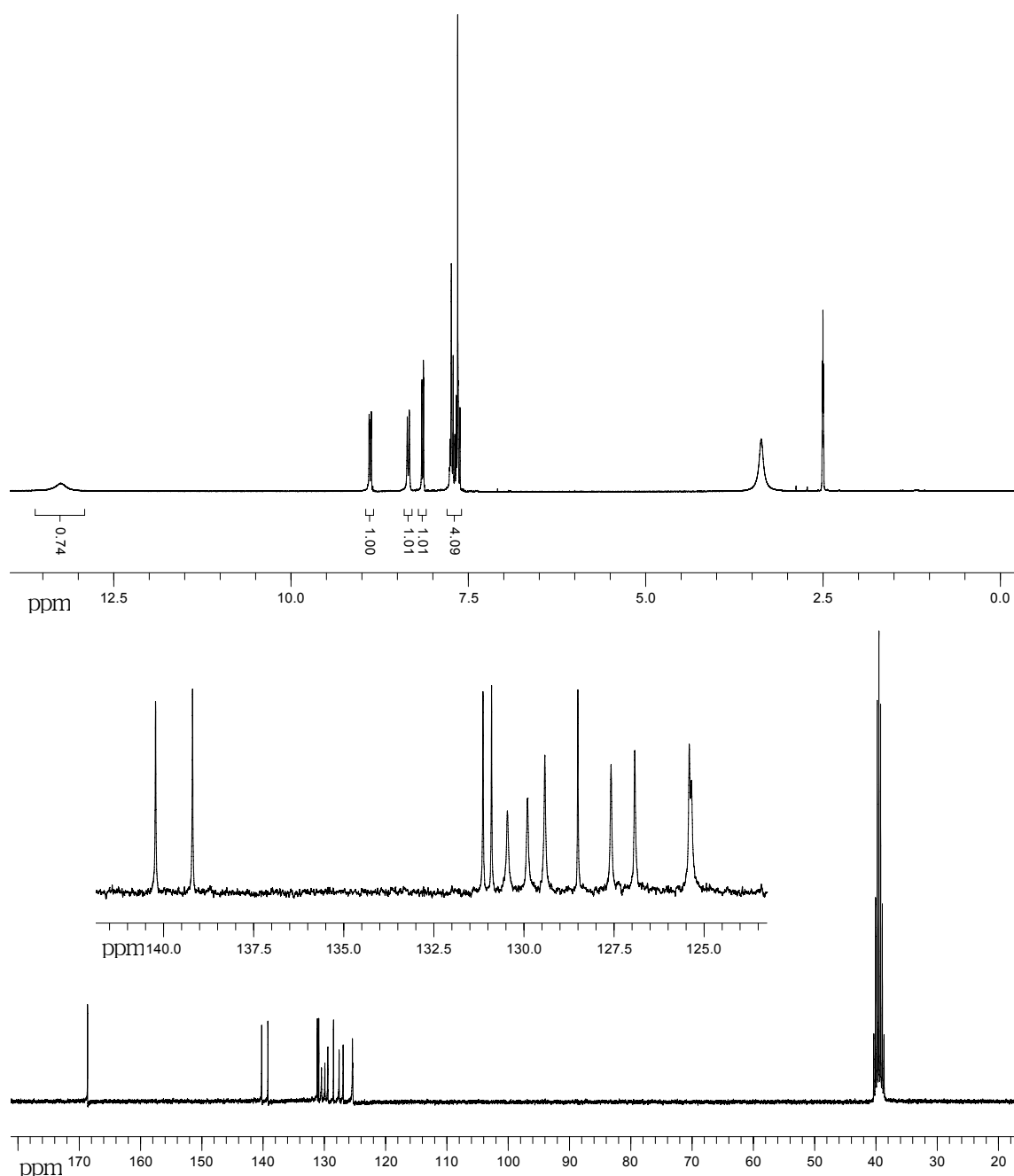


Figure S0. ^1H NMR ($\text{DMSO}-d_6$, 300.0 MHz) and ^{13}C NMR ($\text{DMSO}-d_6$, 75.4 MHz) spectra of the organic linker H_3L .

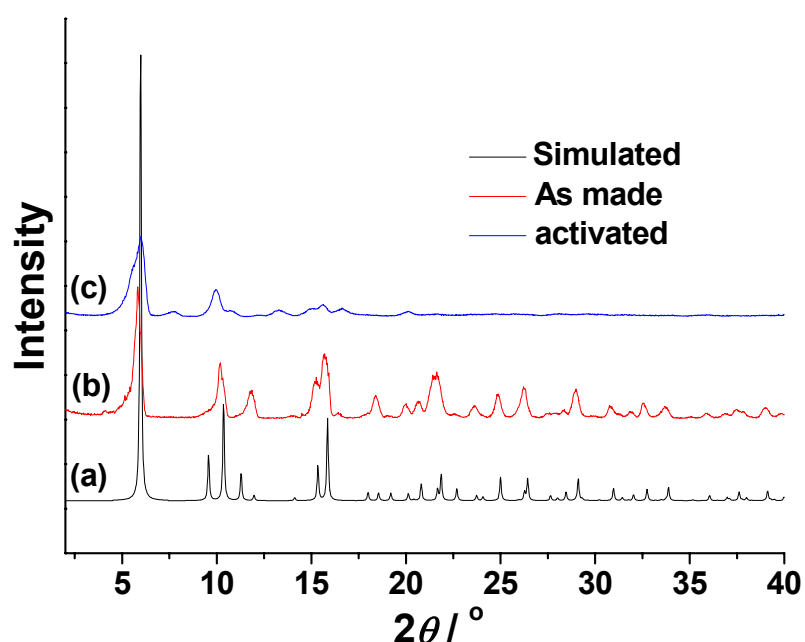


Figure S1. PXRD patterns of as-made **UTSA-30** (b), and activated **UTSA-30a** (c) along with the simulated XRD pattern from the single-crystal structure (a).

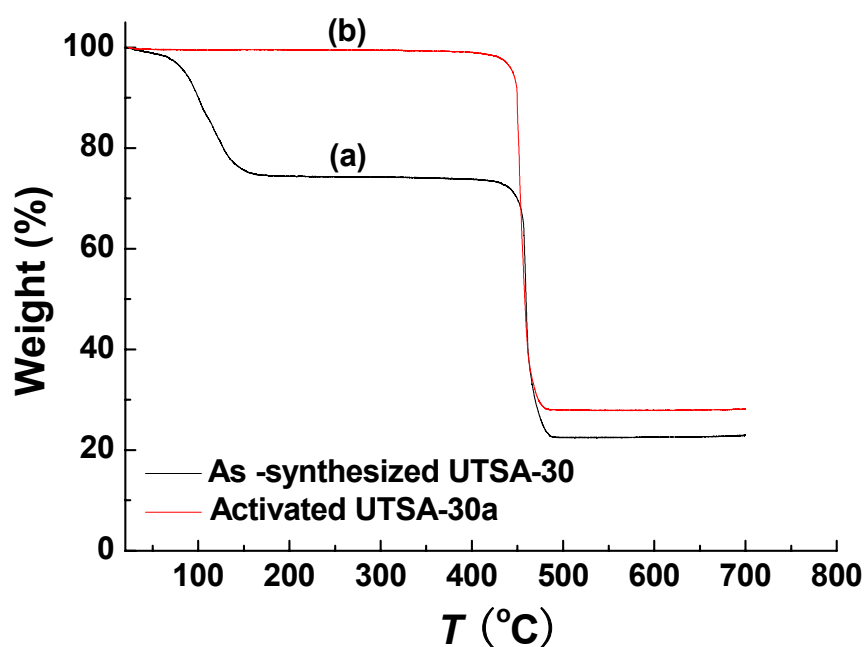


Figure S2. TGA curves of as-synthesized **UTSA-30** (a), and activated **UTSA-30a** (b).

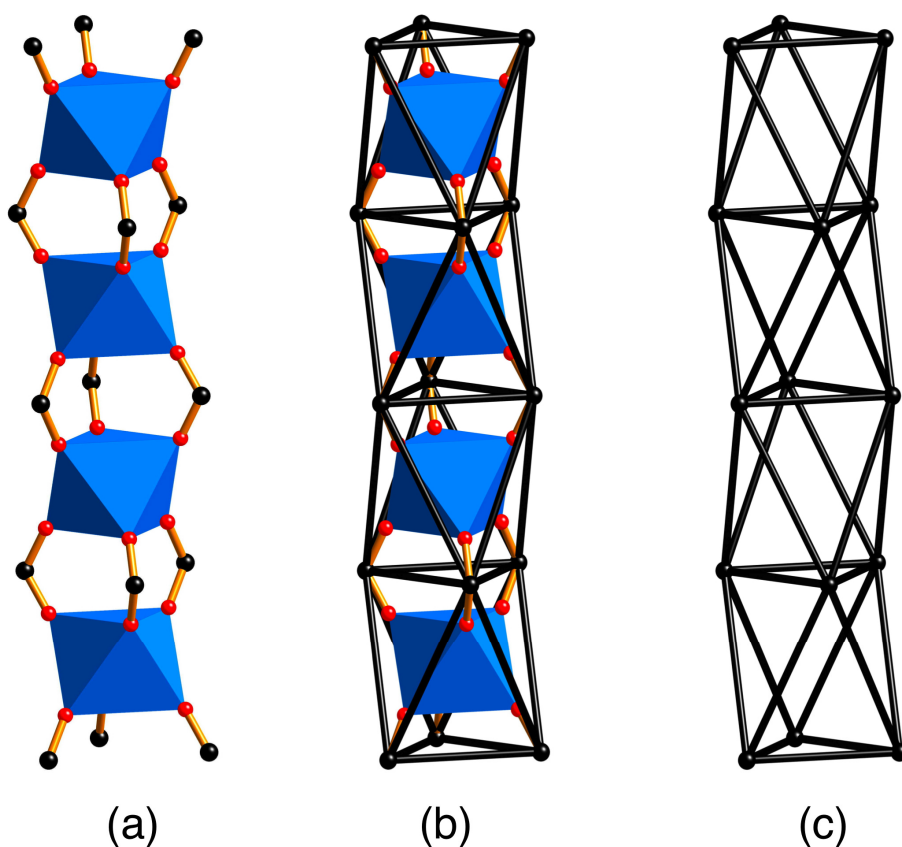


Figure S3. (a) The rod of YbO_6 polyhedra in **UTSA-30**. Oxygen: red, carbon points of extension: black. (b) The envelope of points of extension (black “bonds”). (c) The rod SBU as a column of face-sharing polyhedra.

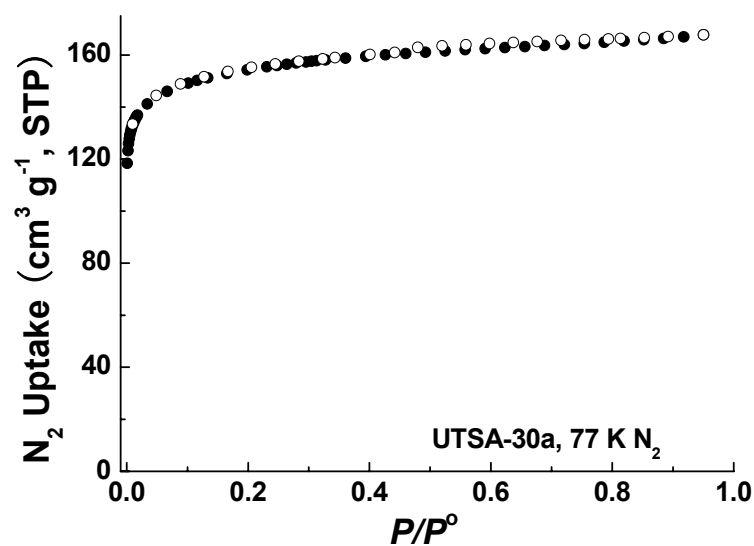
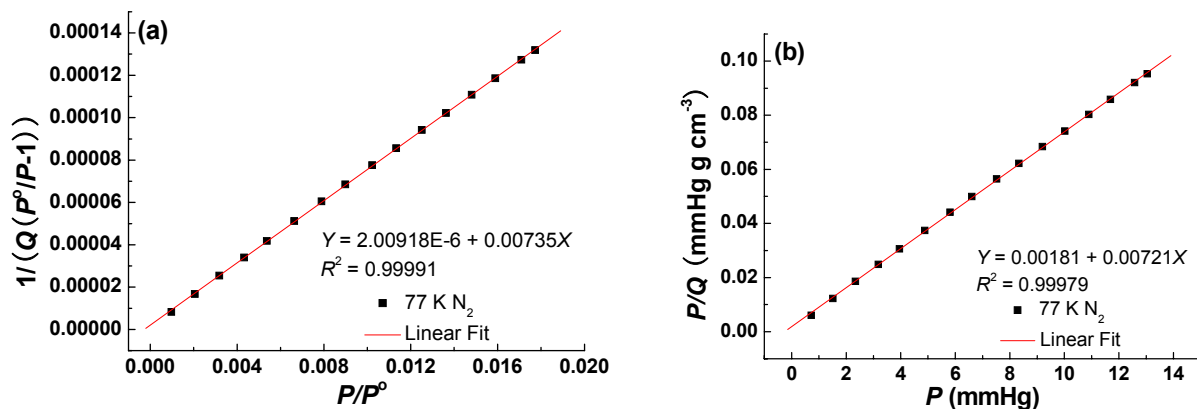


Figure S4. N_2 sorption isotherm of **UTSA-30a** at 77 K. Solid symbols: adsorption, open symbols: desorption.



$$S_{\text{BET}} = (1/(2.00918 \times 10^{-6} + 0.00735))/22414 \times 6.023 \times 10^{23} \times 0.162 \times 10^{-18} = 592.1 \text{ m}^2 \text{ g}^{-1}$$

$$S_{\text{Langmuir}} = (1/0.00721)/22414 \times 6.023 \times 10^{23} \times 0.162 \times 10^{-18} = 603.8 \text{ m}^2 \text{ g}^{-1}.$$

$$\text{BET constant} = 1 + 0.00735/2.00918 \times 10^{-6} = 3659.2$$

$$\text{Langmuir constant} = 0.00721/0.00181 = 3.98 \text{ mmHg}^{-1} = 3.0 \times 10^{-2} \text{ Pa}^{-1}$$

Figure S5. BET (a) and Langmuir (b) plots of UTSA-30a.

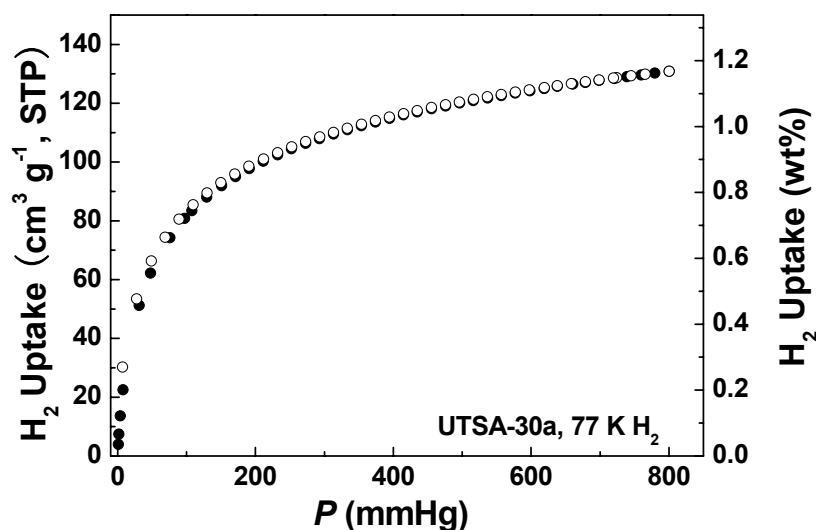


Figure S6. H_2 sorption isotherm of UTSA-30a at 77 K. Solid symbols: adsorption, open symbols: desorption.

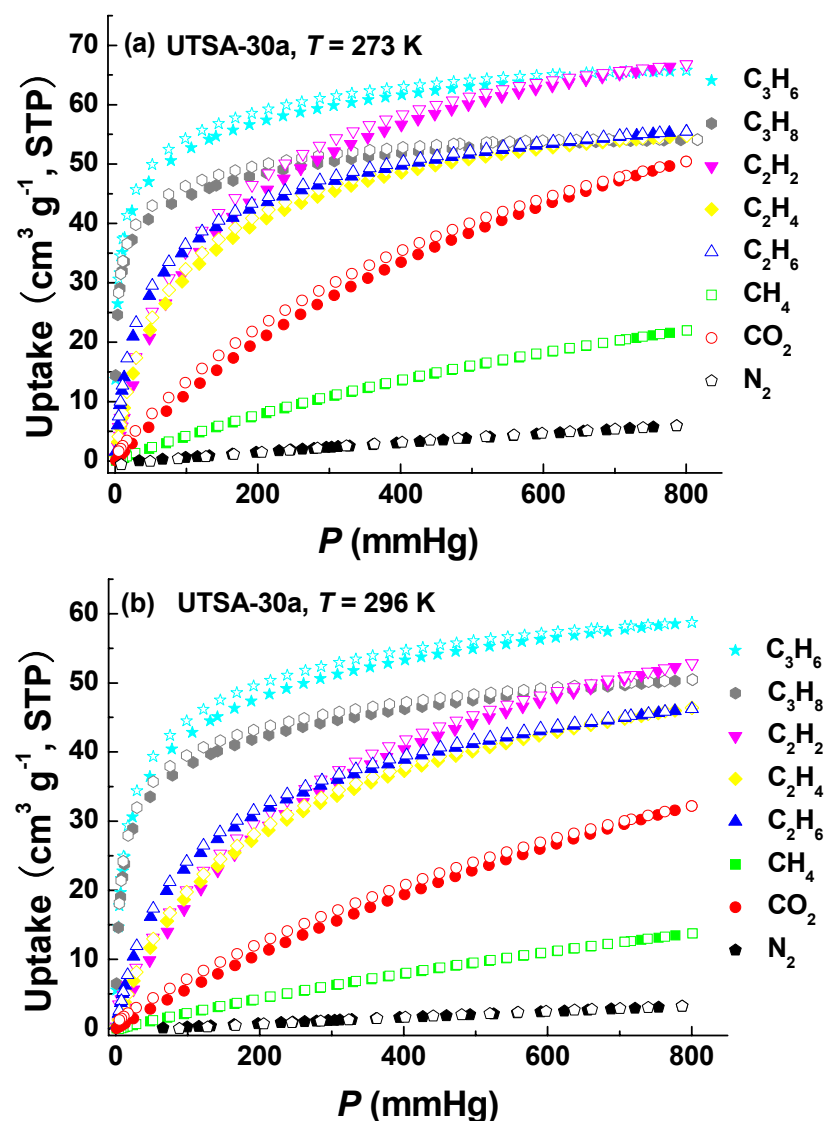


Figure S7. C_3H_6 , C_3H_8 , C_2H_2 , C_2H_4 , C_2H_6 , CH_4 , CO_2 , and N_2 sorption isotherms of **UTSA-30a** at 273 K (a), and 296 K (b). Solid symbols: adsorption, open symbols: desorption.

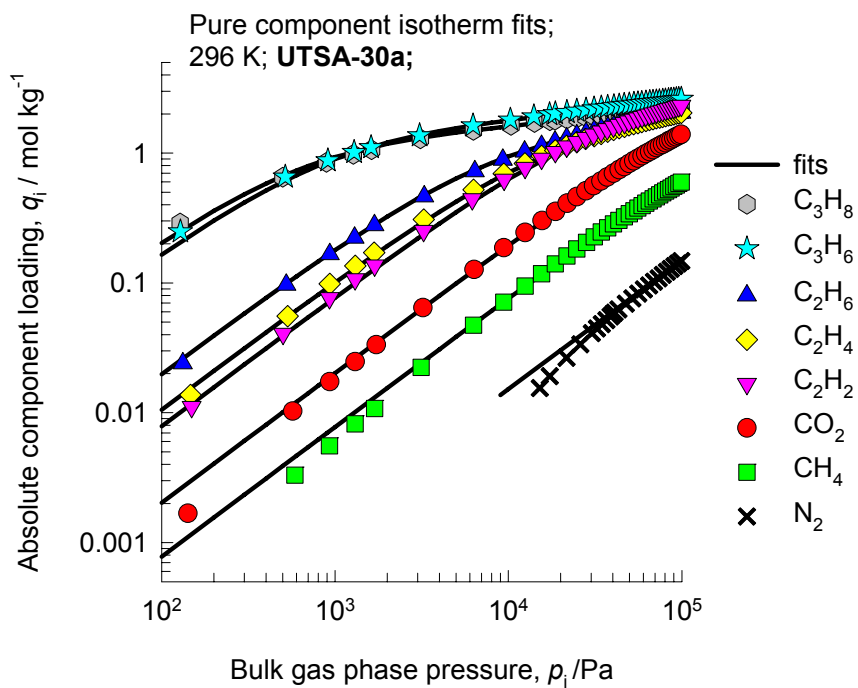


Figure S8. Comparison of absolute component loadings for CH_4 , C_2H_2 , C_2H_4 , C_2H_6 , C_3H_6 , C_3H_8 , CO_2 , and N_2 at 296 K in **UTSA-30a** with the isotherm fits.

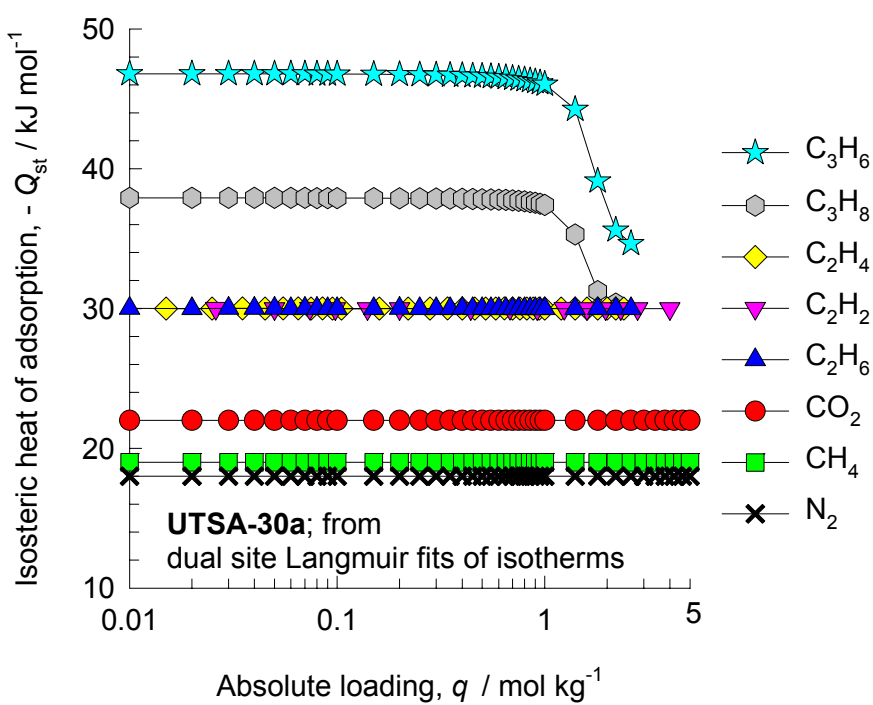


Figure S9. The isosteric heat of adsorption for CH_4 , C_2H_2 , C_2H_4 , C_2H_6 , C_3H_6 , C_3H_8 , CO_2 , and N_2 in **UTSA-30a**. The determination of the Q_{st} is based on analytical differentiation of the pure-component isotherm fits using the methodology described in the work of Mason et al.²¹

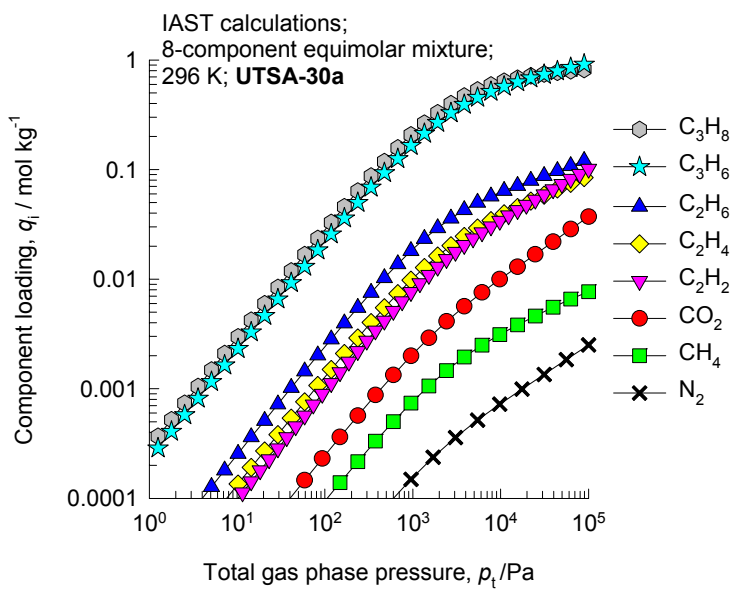


Figure S10. IAST calculations of the component loadings for CH_4 , C_2H_2 , C_2H_4 , C_2H_6 , C_3H_6 , C_3H_8 , CO_2 , and N_2 in an 8-component equimolar mixture as a function of the total bulk gas phase pressure at 296 K.

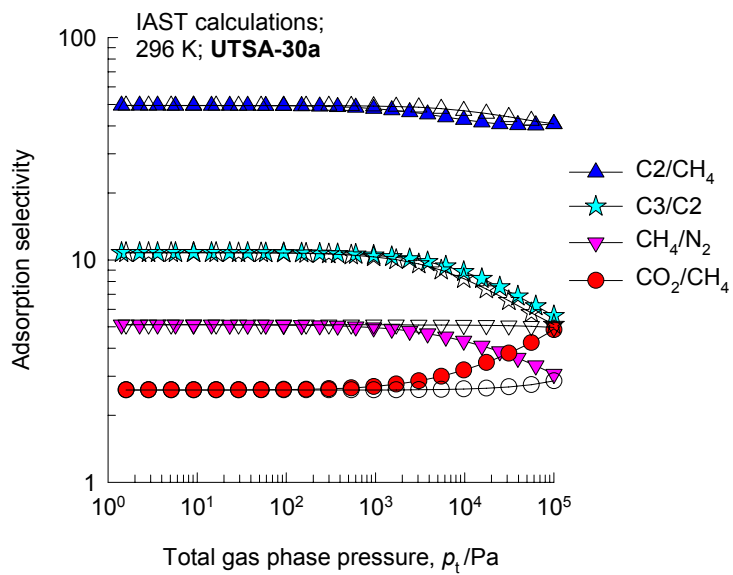


Figure S11. Comparison of IAST calculations of $(\text{C}_2\text{H}_6+\text{C}_2\text{H}_4+\text{C}_2\text{H}_2)/\text{CH}_4$, $(\text{C}_3\text{H}_6+\text{C}_3\text{H}_8)/(\text{C}_2\text{H}_2+\text{C}_2\text{H}_4+\text{C}_2\text{H}_6)$, CO_2/CH_4 , and CH_4/N_2 adsorption selectivities on the basis of loadings in an equimolar 8-component mixture (filled symbols) with (a) IAST calculations for an equimolar 2-component CH_4/CO_2 mixture (open circles), (b) IAST calculations for an equimolar 2-component CH_4/N_2 mixture (open inverted triangles), (c) IAST calculations for an equimolar 4-component $\text{CH}_4/\text{C}_2\text{H}_2/\text{C}_2\text{H}_4/\text{C}_2\text{H}_6$ mixture (open triangles), and (d) IAST calculations for an equimolar 5-component $\text{C}_2\text{H}_2/\text{C}_2\text{H}_4/\text{C}_2\text{H}_6/\text{C}_3\text{H}_6/\text{C}_3\text{H}_8$ mixture (open stars).

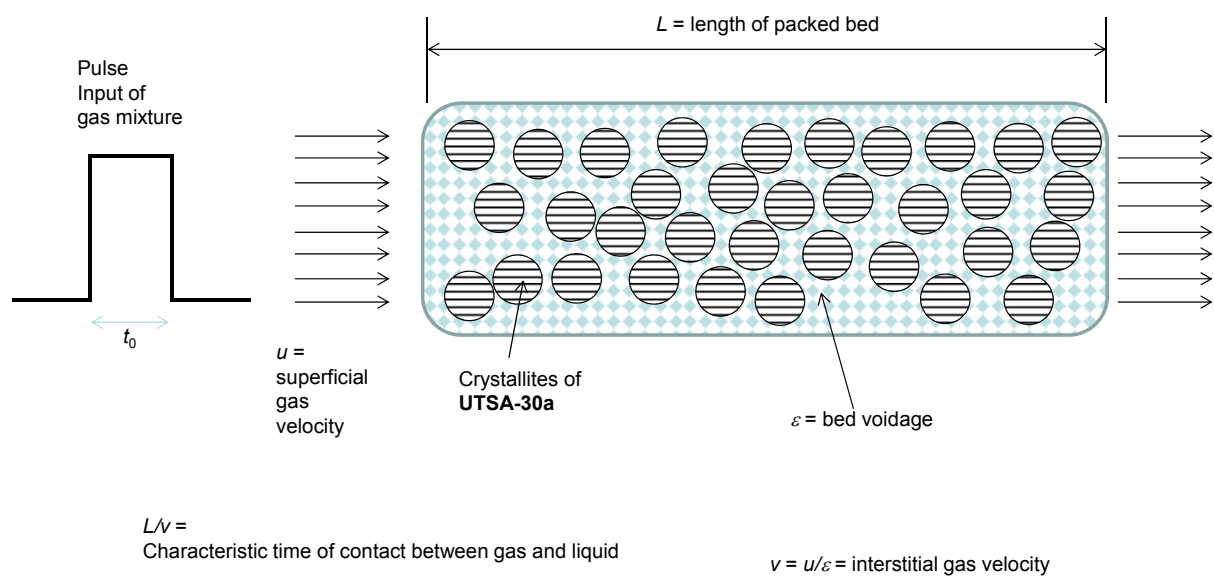


Figure S12. A schematic diagram of a pulse chromatographic adsorber.

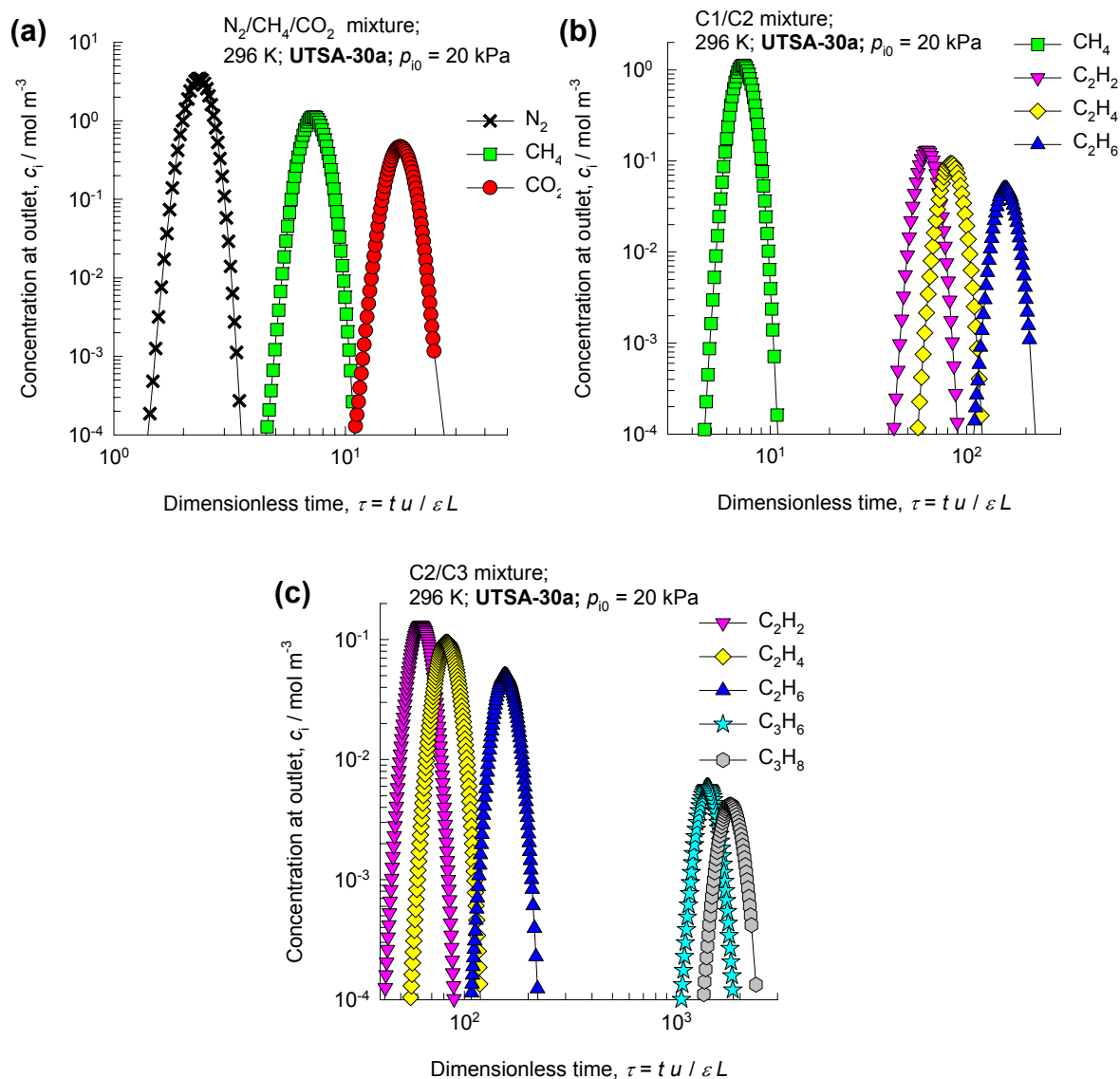


Figure S13. (a) Pulse chromatographic separation of an equimolar 3-component CH₄/CO₂/N₂ mixture using UTSA-30a at 296 K. (b) Pulse chromatographic separation of an equimolar 4-component CH₄/C₂H₂/C₂H₄/C₂H₆ mixture. (c) Pulse chromatographic separation of an equimolar 5-component C₂H₂/C₂H₄/C₂H₆/C₃H₆/C₃H₈ mixture. The x -axis is the dimensionless time. The pulse of the equimolar mixture, with partial pressures of 20 kPa each, is injected for 10 s at the start of the process, and subsequently the adsorbed components are desorbed by use of purge inert gas. It is to be noted that the areas under each of the peaks are identical for each of the species in the mixture. This aspect is not obvious in view of the log-log nature of the plot.

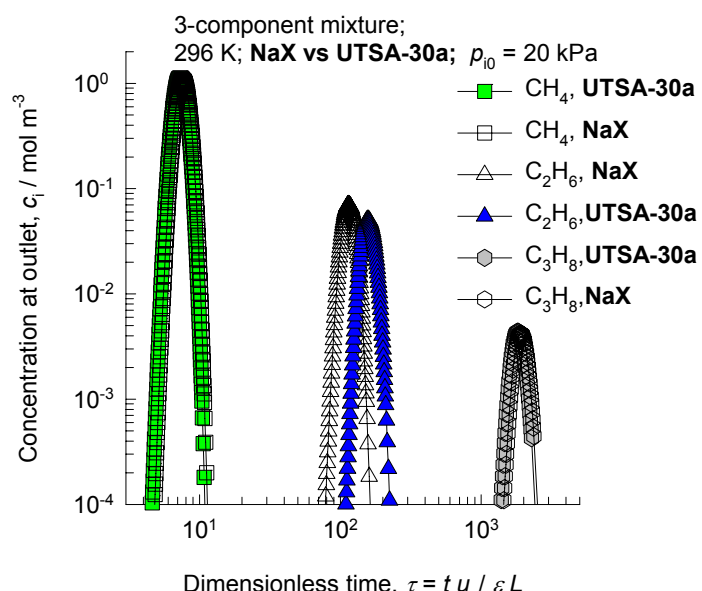


Figure S14. Comparison of the pulse chromatographic separations for an equimolar 3-component $\text{CH}_4/\text{C}_2\text{H}_6/\text{C}_3\text{H}_8$ mixture at 296 K. The filled symbols refer to the simulations for **UTSA-30a**. The open symbols are the corresponding ones for **NaX** zeolite. The x -axis is the dimensionless time. The pulse of the equimolar mixture, with partial pressures of 20 kPa each, is injected for 10 s at the start of the process, and subsequently the adsorbed components are desorbed by use of purge inert gas. It is to be noted that the areas under each of the peaks are identical for each of the species in the mixture. This aspect is not obvious in view of the log-log nature of the plot.

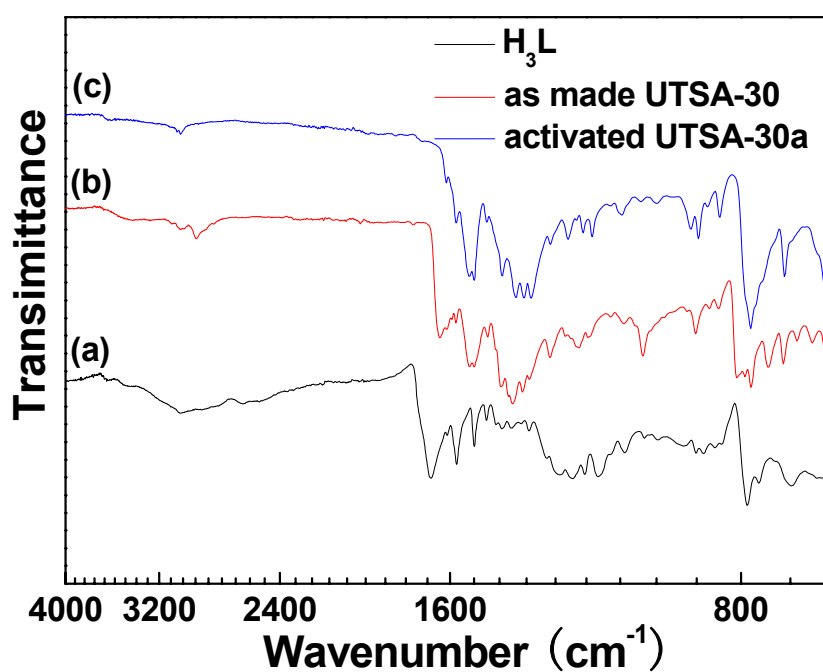


Figure S15. FTIR spectra of H_3L (a), as-made **UTSA-30** (b), and activated **UTSA-30a** (c).

Table S1. Dual-site Langmuir fit parameters for **UTSA-30a**.

Adsorbate	Site A			Site B		
	$q_{A,\text{sat}}$ (mol kg ⁻¹)	b_{A0} (Pa ⁻¹)	E_A (kJ mol ⁻¹)	$q_{B,\text{sat}}$ (mol kg ⁻¹)	b_{B0} (Pa ⁻¹)	E_B (kJ mol ⁻¹)
C ₂ H ₂	3	1.31×10^{-10}	30	4	1.59×10^{-12}	30
C ₂ H ₄	1.2	4.48×10^{-11}	30	1.7	2.85×10^{-10}	30
C ₂ H ₆	1.5	6.4×10^{-10}	30	1.5	3.97×10^{-11}	30
CH ₄	2.7	1.28×10^{-9}	19			
C ₃ H ₆	1.7	5.36×10^{-12}	47	1.4	1.99×10^{-11}	34
C ₃ H ₈	1.5	3.03×10^{-10}	38	1.1	1.11×10^{-10}	30
CO ₂	4.5	5.9×10^{-10}	22			
N ₂	4	2.54×10^{-10}	18			

Table S2. Dual-site Langmuir fit parameters for **NaX** zeolite. These parameter values are valid for 296 K. For CH₄, the parameter values are obtained from the paper by Belmabkhout et al.¹⁸ For C₂H₆, the parameter values are obtained from the paper by Hyun and Danner.¹⁹ For C₃H₈, the parameter values are obtained from the paper by Lamia et al.²⁰

	Site A		Site B	
	$q_{i,A,\text{sat}}$ [mol kg ⁻¹]	$b_{i,A}$ [Pa ⁻¹]	$q_{i,B,\text{sat}}$ [mol kg ⁻¹]	$b_{i,B}$ [Pa ⁻¹]
CH ₄	4	1.08×10^{-7}	5	1.11×10^{-6}
C ₂ H ₆	2.95	3.57×10^{-5}		
C ₃ H ₈	1.1	1.26×10^{-3}	1.1	3.58×10^{-4}

Table S3. Crystal data and structure refinement for **UTSA-30**.

Empirical formula	C ₅₁ H ₄₈ N ₃ O ₉ Yb
Formula weight	1019.98
Temperature (K)	100(2)
Wavelength (Å)	0.71073
Crystal system, space group	Trigonal, <i>P</i> -3m1
	<i>a</i> = 17.0600(17) Å
Unit cell dimensions	<i>b</i> = 17.0600(17) Å
	<i>c</i> = 9.2376(18) Å
	α = 90°
Volume (Å ³)	β = 90°
Z, Calculated density (g cm ⁻³)	γ = 120°
Absorption coefficient (mm ⁻¹)	2328.3(6)
<i>F</i> (000)	2, 1.455
Crystal size (mm)	2.067
θ range for data collection (°)	1034
Limiting indices	0.28 × 0.19 × 0.11
Reflections collected / unique	2.60 to 30.46
Completeness to θ = 30.46°	-19 ≤ <i>h</i> ≤ 20, -20 ≤ <i>k</i> ≤ 19, -12 ≤ <i>l</i> ≤ 12
Absorption correction	8212 / 2457 (<i>R</i> _{int} = 0.0383)
Max. and min. transmission	94.6 %
Refinement method	Semi-empirical from equivalents
Data / restraints / parameters	0.8045 and 0.5952
Goodness-of-fit on <i>F</i> ²	Full-matrix least-squares on <i>F</i> ²
Final <i>R</i> indices (<i>I</i> > 2σ(<i>I</i>))	2457 / 9 / 119
<i>R</i> indices (all data)	1.072
Largest diff. peak and hole (e Å ⁻³)	<i>R</i> ₁ = 0.0496, <i>wR</i> ₂ = 0.1587
CCDC	<i>R</i> ₁ = 0.0722, <i>wR</i> ₂ = 0.1722
	2.067 and -1.390
	894905

Table S4. Gas adsorption properties in the reported porous lanthanide organic frameworks (Ln-MOFs).

MOFs	Formula	Thermal Stability [°C]	BET (Langmuir) [$\text{m}^2 \text{ g}^{-1}$]	V_p [$\text{cm}^3 \text{ g}^{-1}$]	Gas adsorption properties	Ref
MIL-103	Tb(BTB)	400	730-930 (1030-1330)		N_2 adsorption	22
MIL-83(Eu)	Eu ₂ (ADC) ₃	300				23
MOF-76	Tb(BTC)		(334)	0.121	N_2 , Ar, CH ₂ Cl ₂ , C ₆ H ₆ , C ₆ H ₁₂ sorption	24
	Tb(bdc)NO ₃	320		0.032	CO ₂ adsorption	25
	Dy(BTC)	350	655		1.32 wt% H ₂ (77K/1atm)	26
	Gd ₂ (imidc) ₂	290	372		Selective adsorption of H ₂ O over N ₂ , CO ₂ , and MeOH	27
	Na ₆ Eu(L) ₄ Cl	360	426	0.09	CO ₂ adsorption	28
	KHo(C ₂ O ₄) ₂	380	69.1		4.7 wt% CO ₂ (298K/20bar); 0.7 wt% H ₂ (77K/55bar)	29
	Nd(2,5-pydc)(Ac)	400			132 cm ³ /g H ₂ (77K/1atm)	30
	Er ₂ (PDC) ₃ ^a	470	427		N_2 , H ₂ , benzene adsorption	31
	Y ₂ (PDC) ₃ ^a	470	676		N_2 , H ₂ , benzene adsorption	31
	Y(BTC)	450	1080	0.44	1.79 wt% H ₂ (77K/1atm)	32
PCN-17(Dy)	Dy ₄ (TATB) _{8/3} (SO ₄) ₂	500	738	0.31	Selective adsorption of H ₂ and O ₂ over N ₂ and CO	33
PCN-17(Yb)		500	820	0.34	Selective adsorption of H ₂ and O ₂ over N ₂ and CO	34
	Eu ₂ (1,3-BDC) ₃	460	502		N_2 adsorption	35
	Y(BTC)	490			2.1 wt% H ₂ (77K/10atm)	36
	Er ₂ (PDA) ₃ ^b	450		0.027	Selective adsorption of CO ₂ over Ar and N ₂	37
	Tb ₂ (BDC) ₃	450		0.099	Sorption of H ₂ O and NH ₃	38
	La(BTB)	560	1014		Breathing effect of CO ₂	39
	Y ₂ (BPDC) ₃	350	(134)		N_2 , Ar, CO ₂ , MeOH and H ₂ O adsorption	40
	Gd ₂ (FDA) ₃	400	438(726)		0.8 wt% H ₂ (77K/1atm); 56 cm ³ /g CO ₂ (273K/1atm)	41
	La(epia)	400	(147)		23 cm ³ /g CO ₂ (273K/P/P ⁰ = 0.3)	42
	Nd(TPO)	500	793	0.344	0.89 wt% H ₂ (77K/1atm); 125 cm ³ /g CO ₂ (196K/1atm)	43
	Yb(BPT)	450	515.6	0.291	C ₂ H ₂ /CH ₄ , CO ₂ /CH ₄ , MeOH/EtOH	44
	Tb(TATB)	320	1783(3855)		18 mmol/g CO ₂ (298K/45bar)	45
	Er ₂ (TBDC) ₃ (phen) ₂		(141)		Selective adsorption of CO ₂ and H ₂ over N ₂ and Ar	46
	Tb ₃ (BDC) _{4.5}	400			H ₂ O sorption	47
	Gd(BTC)	420	585(773)	0.283	92 cm ³ /g CO ₂ (273K/1atm)	48
	EuL(NO ₃) ₃	200			Selective adsorption of water over organic solvents	49

BTB = 1,3,5-benzenetrisbenzoate; bdc = 1,4-benzenedicarboxylate; H₂ADC = 1,3-adamantanedicarboxylic acid; H₃imidc = 4,5-imidazoledicarboxylic acid; L = 4,4'-disulfo-2,2'-bipyridine-N,N'-dioxide; H₂2,5-pydc = pyridine-2,5-dicarboxylic acid; ^a PDC = pyridine-3,5-dicarboxylate; TATB = 4,4',4''-s-triazine-2,4,6-triyl-tribenzozate; ^b H₂PDA = 1,4-phenyldiacetic acid; H₂FDA = thiophene-2,5-dicarboxylic acid; H₃cpia = 5-(4-carboxyphenoxy)isophthalic acid; H₃TPO = tris(4-carboxylphenyl)phosphineoxide; BPT = biphenyl-3,4',5-tricarboxylate; H₄TBDC = 2,3,5,6-tetramethyl-1,4-benzenedicarboxylic acid.

9. Reference

- (1) Repine, J. T.; Johnson, D. S.; White, A. D.; Favor, D. A.; Stier, M. A.; Yip, J.; Rankin, T.; Ding, Q.; Maiti, S. N. Synthesis of monofluorinated 1-(naphthalen-1-yl)piperazines, *Tetrahedron Lett.* **2007**, *48*, 5539-5541.
- (2) Ishiyama, T.; Murata, M.; Miyaura, N. Palladium(0)-Catalyzed Cross-Coupling Reaction of Alkoxydiboron with Haloarenes: A Direct Procedure for Arylboronic Esters, *J. Org. Chem.* **1995**, *60*, 7508-7510.
- (3) He, Y.; Zhang, Z.; Xiang, S.; Fronczek, F. R.; Krishna, R.; Chen, B. A robust doubly interpenetrated metal-organic framework constructed from a novel aromatic tricarboxylate for highly selective separation of small hydrocarbons, *Chem. Commun.* **2012**, *48*, 6493-6495.
- (4) Myers, A. L.; Prausnitz, J. M. Thermodynamics of mixed gas adsorption, *A.I.Ch.E.J.* **1965**, *11*, 121-130.
- (5) Herm, Z. R.; Swisher, J. A.; Smit, B.; Krishna, R.; Long, J. R. Metal-Organic Frameworks as Adsorbents for Hydrogen Purification and Pre-Combustion Carbon Dioxide Capture, *J. Am. Chem. Soc.* **2011**, *133*, 5664-5667.
- (6) Krishna, R.; van Baten, J. M. Investigating the potential of **MgMOF-74** membranes for CO₂ capture, *J. Membr. Sci.* **2011**, *377*, 249-260.
- (7) Krishna, R.; van Baten, J. M. In silico screening of metal-organic frameworks in separation applications, *Phys. Chem. Chem. Phys.* **2011**, *13*, 10593-10616.
- (8) Krishna, R.; van Baten, J. M. Maxwell-Stefan modeling of slowing-down effects in mixed gas permeation across porous membranes, *J. Membr. Sci.* **2011**, *383*, 289-300.
- (9) Wu, H.; Yao, K.; Zhu, Y.; Li, B.; Shi, Z.; Krishna, R.; Li, J. Cu-TDPAT, an *rht*-type Dual-Functional Metal–Organic Framework Offering Significant Potential for Use in H₂ and Natural Gas Purification Processes Operating at High Pressures, *J. Phys. Chem. C* **2012**, DOI: 10.1021/jp3046356.
- (10) Krishna, R.; Long, J. R. Screening metal-organic frameworks by analysis of transient breakthrough of gas mixtures in a fixed bed adsorber, *J. Phys. Chem. C* **2011**, *115*, 12941-12950.
- (11) Krishna, R.; van Baten, J. M. A comparison of the CO₂ capture characteristics of zeolites and metal-organic frameworks, *Sep. Purif. Technol.* **2012**, *87*, 120-126.
- (12) Krishna, R.; Baur, R. Modelling issues in zeolite based separation processes, *Sep. Purif. Technol.* **2003**, *33*, 213-254.
- (13) Krishna, R.; Baur, R. Diffusion, Adsorption and Reaction in Zeolites: Modelling and Numerical Issues, <http://www.science.uva.nl/research/cr/zeolite/>, University of Amsterdam, Amsterdam, 11 November 2003.
- (14) He, Y.; Krishna, R.; Chen, B. Metal-Organic Frameworks with Potential for Energy-Efficient Adsorptive Separation of Light Hydrocarbons, *Energy Environ. Sci.* **2012**, DOI: 10.1039/C2EE22858K.
- (15) van den Broeke, L. J. P.; Krishna, R. Experimental Verification of the Maxwell-Stefan Theory for Micropore Diffusion, *Chem. Eng. Sci.* **1995**, *50*, 2507-2522.
- (16) Walton, K. S.; LeVan, M. D. Consistency of Energy and Material Balances for Bidisperse Particles in Fixed-Bed Adsorption and Related Applications, *Ind. Eng. Chem. Res.* **2003**, *42*, 6938-6948.

- (17) Bloch, E. D.; Queen, W. L.; Krishna, R.; Zadrozny, J. M.; Brown, C. M.; Long, J. R. Hydrocarbon Separations in a Metal-Organic Framework with Open Iron(II) Coordination Sites, *Science* **2012**, *335*, 1606-1610.
- (18) Belmabkhout, Y.; Pirngruber, G.; Jolimaitre, E.; Methivier, A. A complete experimental approach for synthesis gas separation studies using static gravimetric and column breakthrough experiments, *Adsorption* **2007**, *13*, 341-349.
- (19) Hyun, S. H.; Danner, R. P. Equilibrium Adsorption of Ethane, Ethylene, Isobutane, Carbon Dioxide, and Their Binary Mixtures on 13X Molecular Sieves, *J. Chem. Eng. Data* **1982**, *27*, 196-200.
- (20) Lamia, N.; Granato, M. A.; Gomes, P. S. A.; Grande, C. A.; Wolff, L.; Leflaive, P.; Leinekugel-le-Cocq, D.; Rodrigues, A. E. Propane/Propylene Separation by Simulated Moving Bed II. Measurement and Prediction of Binary Adsorption Equilibria of Propane, Propylene, Isobutane, and 1-Butene on 13X Zeolite, *Sep. Sci. and Technol.* **2009**, *44*, 1485-1509.
- (21) Mason, J. A.; Sumida, K.; Herm, Z. R.; Krishna, R.; Long, J. R. Evaluating Metal-Organic Frameworks for Post-Combustion Carbon Dioxide Capture via Temperature Swing Adsorption, *Energy Environ. Sci.* **2011**, *3*, 3030-3040.
- (22) Devic, T.; Serre, C.; Audebrand, N.; Marrot, J.; Férey, G. MIL-103, A 3-D Lanthanide-Based Metal Organic Framework with Large One-Dimensional Tunnels and A High Surface Area, *J. Am. Chem. Soc.* **2005**, *127*, 12788-12789.
- (23) Millange, F.; Serre, C.; Marrot, J.; Gardant, N.; Pellé, F.; Férey, G. Synthesis, structure and properties of a three-dimensional porous rare-earth carboxylate MIL-83(Eu): Eu₂(O₂C-C₁₀H₁₄-CO₂)₃, *J. Mater. Chem.* **2004**, *14*, 642-645.
- (24) Rosi, N. L.; Kim, J.; Eddaoudi, M.; Chen, B.; O'Keeffe, M.; Yaghi, O. M. Rod Packings and Metal-Organic Frameworks Constructed from Rod-Shaped Secondary Building Units, *J. Am. Chem. Soc.* **2005**, *127*, 1504-1518.
- (25) Reineke, T. M.; Eddaoudi, M.; O'Keeffe, M.; Yaghi, O. M. A Microporous Lanthanide-Organic Framework, *Angew. Chem. Int. Ed.* **1999**, *38*, 2590-2594.
- (26) Guo, X.; Zhu, G.; Li, Z.; Sun, F.; Yang, Z.; Qiu, S. A lanthanide metal-organic framework with high thermal stability and available Lewis-acid metal sites, *Chem. Commun.* **2006**, 3172-3174.
- (27) Maji, T. K.; Mostafa, G.; Chang, H.-C.; Kitagawa, S. Porous lanthanide-organic framework with zeolite-like topology, *Chem. Commun.* **2005**, 2436-2438.
- (28) Chandler, B. D.; Yu, J. O.; Cramb, D. T.; Shimizu, G. K. H., Series of Lanthanide-Alkali Metal-Organic Frameworks Exhibiting Luminescence and Permanent Microporosity, *Chem. Mater.* **2007**, *19*, 4467-4473.
- (29) Mohapatra, S.; Hembram, K. P. S. S.; Waghmare, U.; Maji, T. K. Immobilization of Alkali Metal Ions in a 3D Lanthanide-Organic Framework: Selective Sorption and H₂ Storage Characteristics, *Chem. Mater.* **2009**, *21*, 5406-5412.
- (30) Huang, Y.-G.; Jiang, F.-L.; Yuan, D.-Q.; Wu, M.-Y.; Gao, Q.; Wei, W.; Hong, M.-C. A Prototypical Zeolitic Lanthanide-Organic Framework with Nanotubular Structure, *Cryst. Growth Des.* **2008**, *8*, 166-168.
- (31) Jia, J.; Lin, X.; Blake, A. J.; Champness, N. R.; Hubberstey, P.; Shao, L.; Walker, G.; Wilson, C.; Schröder, M. Triggered Ligand Release Coupled to Framework Rearrangement: Generating Crystalline Porous Coordination Materials, *Inorg. Chem.* **2006**, *45*, 8838-8840.
- (32) Jiang, H.-L.; Tsumori, N.; Xu, Q. A Series of (6,6)-Connected Porous Lanthanide-Organic

- Framework Enantiomers with High Thermostability and Exposed Metal Sites: Scalable Syntheses, Structures, and Sorption Properties, *Inorg. Chem.* **2010**, *49*, 10001-10006.
- (33) Ma, S.; Yuan, D.; Wang, X.-S.; Zhou, H.-C. Microporous Lanthanide Metal-Organic Frameworks Containing Coordinatively Linked Interpenetration: Syntheses, Gas Adsorption Studies, Thermal Stability Analysis, and Photoluminescence Investigation, *Inorg. Chem.* **2009**, *48*, 2072-2077.
- (34) Ma, S.; Wang, X.-S.; Yuan, D.; Zhou, H.-C. A Coordinatively Linked Yb Metal-Organic Framework Demonstrates High Thermal Stability and Uncommon Gas-Adsorption Selectivity, *Angew. Chem. Int. Ed.* **2008**, *47*, 4130-4133.
- (35) Wang, G.; Song, T.; Fan, Y.; Xu, J.; Wang, M.; Wang, L.; Zhang, L.; Wang, L. A porous lanthanide metal-organic framework with luminescent property, nitrogen gas adsorption and high thermal stability, *Inorg. Chem. Commun.* **2010**, *13*, 95-97.
- (36) Luo, J.; Xu, H.; Liu, Y.; Zhao, Y.; Daemen, L. L.; Brown, C.; Timofeeva, T. V.; Ma, S.; Zhou, H.-C. Hydrogen Adsorption in a Highly Stable Porous Rare-Earth Metal-Organic Framework: Sorption Properties and Neutron Diffraction Studies, *J. Am. Chem. Soc.* **2008**, *130*, 9626-9627.
- (37) Pan, L.; Adams, K. M.; Hernandez, H. E.; Wang, X.; Zheng, C.; Hattori, Y.; Kaneko, K. Porous Lanthanide-Organic Frameworks: Synthesis, Characterization, and Unprecedented Gas Adsorption Properties, *J. Am. Chem. Soc.* **2003**, *125*, 3062-3067.
- (38) Reineke, T. M.; Eddaoudi, M.; Fehr, M.; Kelley, D.; Yaghi, O. M. From Condensed Lanthanide Coordination Solids to Microporous Frameworks Having Accessible Metal Sites, *J. Am. Chem. Soc.* **1999**, *121*, 1651-1657.
- (39) Mu, B.; Li, F.; Huang, Y.; Walton, K. S. Breathing effects of CO₂ adsorption on a flexible 3D lanthanide metal-organic framework, *J. Mater. Chem.* **2012**, *22*, 10172-10178.
- (40) Chen, J.; Chen, Z.; Yu, T.; Weng, L.; Tu, B.; Zhao, D., Synthesis, structure, and adsorption properties of a three-dimensional porous yttrium-organic coordination network, *Micropor. Mesopor. Mater.* **2007**, *98*, 16-20.
- (41) HuanHuan, L.; Zheng, N.; Tian, H.; ZhenJie, Z.; Wei, S.; Peng, C. A microporous lanthanide metal-organic framework containing channels: Synthesis, structure, gas adsorption and magnetic properties, *Sci. China Chem.* **2011**, *54*, 1423-1429.
- (42) Lama, P.; Aijaz, A.; Neogi, S.; Barbour, L. J.; Bharadwaj, P. K. Microporous La(III) Metal-Organic Framework Using a Semirigid Tricarboxylic Ligand: Synthesis, Single-Crystal to Single-Crystal Sorption Properties, and Gas Adsorption Studies, *Cryst. Growth Des.* **2010**, *10*, 3410-3417.
- (43) Lee, W. R.; Ryu, D. W.; Lee, J. W.; Yoon, J. H.; Koh, E. K.; Hong, C. S. Microporous Lanthanide-Organic Frameworks with Open Metal Sites: Unexpected Sorption Propensity and Multifunctional Properties, *Inorg. Chem.* **2010**, *49*, 4723-4725.
- (44) Guo, Z.; Xu, H.; Su, S.; Cai, J.; Dang, S.; Xiang, S.; Qian, G.; Zhang, H.; O'Keeffe, M.; Chen, B. A robust near infrared luminescent ytterbium metal-organic framework for sensing of small molecules, *Chem. Commun.* **2011**, *47*, 5551-5553.
- (45) Park, Y. K.; Choi, S. B.; Kim, H.; Kim, K.; Won, B.-H.; Choi, K.; Choi, J.-S.; Ahn, W.-S.; Won, N.; Kim, S.; Jung, D. H.; Choi, S.-H.; Kim, G.-H.; Cha, S.-S.; Jhon, Y. H.; Yang, J. K.; Kim, J. Crystal Structure and Guest Uptake of a Mesoporous Metal-Organic Framework Containing Cages of 3.9 and 4.7 nm in Diameter, *Angew. Chem. Int. Ed.* **2007**, *46*, 8230-8233.
- (46) He, H.; Yuan, D.; Ma, H.; Sun, D.; Zhang, G.; Zhou, H.-C. Control over Interpenetration in

Lanthanide-Organic Frameworks: Synthetic Strategy and Gas-Adsorption Properties, *Inorg. Chem.* **2010**, *49*, 7605-7607.

- (47) Guo, X.; Zhu, G.; Sun, F.; Li, Z.; Zhao, X.; Li, X.; Wang, H.; Qiu, S. Synthesis, Structure, and Luminescent Properties of Microporous Lanthanide Metal-Organic Frameworks with Inorganic Rod-Shaped Building Units, *Inorg. Chem.* **2006**, *45*, 2581-2587.
- (48) Xie, L.-H.; Wang, Y.; Liu, X.-M.; Lin, J.-B.; Zhang, J.-P.; Chen, X.-M. Crystallographic studies into the role of exposed rare earth metal ion for guest sorption, *CrystEngComm* **2011**, *13*, 5849-5857.
- (49) Zheng, X.-D.; Zhang, M.; Jiang, L.; Lu, T.-B. A pair of 3D homochiral metal-organic frameworks: spontaneous resolution, single-crystal-to-single-crystal transformation and selective adsorption properties, *Dalton Trans.* **2012**, *41*, 1786-1791.

10. Notation

b_A	dual-Langmuir constant for species i at adsorption site A, Pa $^{-1}$
b_B	dual-Langmuir constant for species i at adsorption site B, Pa $^{-1}$
L	length of packed bed adsorber, m
n	number of species in the mixture, dimensionless
p_i	partial pressure of species i in mixture, Pa
p_{i0}	partial pressure of species i at inlet to fixed bed, Pa
p_t	total system pressure, Pa
q_i	component molar loading of species i , mol kg $^{-1}$
q_t	total molar loading in mixture, mol kg $^{-1}$
$q_{\text{sat},A}$	saturation loading of site A, mol kg $^{-1}$
$q_{\text{sat},B}$	saturation loading of site B, mol kg $^{-1}$
Q_{st}	isosteric heat of adsorption, J mol $^{-1}$
R	gas constant, 8.314 J mol $^{-1}$ K $^{-1}$
t	time, s
t_0	duration of pulse, s
T	absolute temperature, K
u	superficial gas velocity in packed bed, m s $^{-1}$
u_0	superficial gas velocity at inlet to packed bed, m s $^{-1}$
v	interstitial gas velocity in packed bed, m s $^{-1}$
x_i	mole fraction of species i in adsorbed phase, dimensionless
z	distance along the adsorber, m

Greek letters

ε	voidage of packed bed, dimensionless
μ_i	molar chemical potential, J mol ⁻¹
ν	exponent in dual-Langmuir-Freundlich isotherm, dimensionless
ρ	framework density, kg m ⁻³
τ	time, dimensionless

Subscripts

0	referring to conditions at inlet to adsorber
i	referring to component <i>i</i>
A	referring to site A
B	referring to site B
t	referring to total mixture